

Quantum Geometry Induced Kekulé Superconductivity in Haldane phases

Yafis Barlas,^{1,*} Fan Zhang,² and Enrico Rossi³

¹Department of Physics, University of Nevada, Reno, Nevada 89557, USA

²Department of Physics, University of Texas at Dallas, Richardson, Texas 75080, USA

³Department of Physics, William and Mary, Williamsburg, Virginia 21387, USA

Chiral two-dimensional electron gases, which capture the electronic properties of graphene and rhombohedral graphene systems, exhibit singular momentum-space vortices and are susceptible to interaction-induced topological Haldane phases. Here, we investigate pairing interactions in the inversion-symmetric Haldane phases of chiral two-dimensional electron gases. We demonstrate that the nontrivial band topology of the Haldane phases enhances intra-valley ($\mathbf{Q} = \pm 2\mathbf{K}_D$) pair susceptibility relative to inter-valley ($\mathbf{Q} = 0$) pair susceptibility, favoring the emergence of a lattice-scale pair-density wave order. When longitudinal acoustic phonons mediate the pairing interaction, the system supports a chiral Kekulé superconducting order at low densities. At higher densities, the phase diagram depends on the parity of the chiral index J . For even parity an s -wave Kekulé order appears, while for odd parity we find a $\mathbf{Q} = 0$ valley triplet chiral- J and a valley singlet s -wave order at different densities. Our findings are relevant to superconductivity in rhombohedral graphene and Kagome metals.

While significant progress has been made in understanding unconventional superconductivity [1–11] in spin Chern bands of twisted two-dimensional (2D) crystals, the presence of a moiré superlattice often complicates the identification of the underlying mechanisms [12–29]. For instance, it remains unresolved whether the observed superconductivity originates predominantly from band-projected interactions or from novel pairing instabilities intrinsic to topological bands [30–34]. Alternatively, multi-layer rhombohedral graphene (RG) has emerged as a promising platform, displaying superconducting phenomenology [35–43] that appears to be as rich as that of twisted 2D crystals [44–47], but without the complexity of a moiré potential. Notably, in RG, superconductivity can even be hosted by a spin-polarized valley Chern band [35–43, 45, 48], which underscores the necessity to understand the interplay of band geometry and pairing interactions [49].

In ordinary metals, the pair susceptibility typically diverges at zero center-of-mass momentum ($\mathbf{Q} = 0$), favoring uniform superconductivity over finite-momentum pairing at weak coupling [50–52]. In contrast, this Letter demonstrates that the nontrivial topology of a Chern band qualitatively modifies this picture. Our conclusions are based on the analysis of superconducting pairing within a Chern band realized in chiral two-dimensional electron gases (C2DEGs). Specifically, we show that in a spin-polarized half-metal phase of RG, the band-projected intra-valley pair susceptibility with pair momentum $\mathbf{Q} = \pm 2\mathbf{K}_D$ is enhanced relative to the inter-valley pair susceptibility with $\mathbf{Q} = 0$, and depends on the ratio m/μ , where μ is the Fermi energy and m is an interaction-induced Haldane mass [53]. Since this enhancement occurs at high-symmetry points in the Brillouin zone, it naturally favors a lattice-scale pair density wave (PDW) order, previously identified as a Kekulé superconductor in a different context [54].

This enhancement arises from the coherence factors of the Bloch wavefunctions in the Haldane phase [55], which can be visualized using the \hat{z} -component of pseudo-spinor field defined by the Hamiltonian on the Bloch sphere, as illustrated in Fig. 1. In the case of intra-valley pairing as depicted in Fig. 1 a), the \hat{z} -component pseudo-spinors point in the same

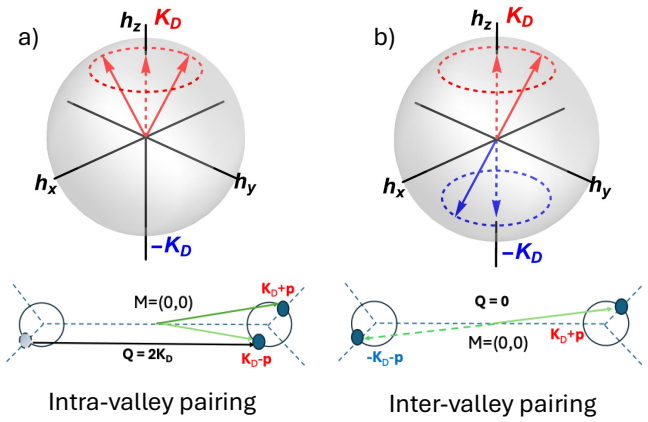


FIG. 1. Hamiltonian pseudo-spinor field $\hat{\mathbf{h}}$ on the Bloch sphere for a) intra-valley pairing and b) inter-valley pairing in the Haldane phase, with the Fermi surface projection indicated by the dotted red (blue) circles for \mathbf{K}_D ($-\mathbf{K}_D$) valleys. The projections of $\hat{\mathbf{h}}$ onto the \hat{z} -direction for intra-valley pairs \mathbf{p} and $-\mathbf{p}$ are parallel, whereas they are anti-parallel for inter-valley pairs \mathbf{p} and $-\mathbf{p}$. This spinor structure of the Haldane phase results in the suppression of the coherence factors of the inter-valley pair susceptibility (see text for details).

direction, resulting in constructive interference. In contrast, for inter-valley pairing shown in Fig. 1 b), the pseudo-spinors point in opposite directions, leading to destructive interference and a corresponding suppression of the inter-valley pair susceptibility. Overall, the pair susceptibility and superconducting phase diagram depend on the parity of the chiral index J . When longitudinal acoustic phonons mediate the pairing interaction, the system supports a chiral Kekulé superconducting order for low densities n_e . For even values of J the system transitions to an s -wave Kekulé superconducting order when $n_e > n_{e,2}$, and chiral Kekulé superconducting order appears for $n_e > n_{e,2}$. For odd values of J , a π -phase chiral Kekulé superconducting order appears when $n_e < n_{e,1}$, while in the density regime $n_{e,1} < n_e < n_{e,2}$, we find a $\mathbf{Q} = 0$ valley triplet chiral superconducting state and a valley-singlet s -wave

superconductor for $n_e > n_{e,2}$. The chiral superconducting order arises from projected interactions within the topological bands, thereby further reflecting the underlying geometric features of the Haldane phase of C2DEGs.

Model.—The continuum model Hamiltonian of a C2DEG with a Chern number J on a projected bipartite lattice is

$$H_0 = \zeta_J p^J \left(\hat{\sigma}_x \cos(J\varphi_{\mathbf{p}}) + \tau_z \hat{\sigma}_y \sin(J\varphi_{\mathbf{p}}) \right) + m \hat{\sigma}_z \tau_z, \quad (1)$$

where the Pauli matrices $\hat{\sigma}_i$ act on the pseudospinor $\psi^\dagger = (\psi_A^\dagger, \psi_B^\dagger)$, (A, B) are sublattice degrees of freedom to be specified below, $\tau_z = \pm 1$ denote the valleys associated with the Dirac points located at the corners of the hexagonal Brillouin zone (BZ) $\pm \mathbf{K}_D$, $\mathbf{p} = (p_x, p_y)$ is the momentum measured from the Dirac points with $\varphi_{\mathbf{p}} = \tan^{-1}(p_y/p_x)$, and $p = \sqrt{p_x^2 + p_y^2}$. We choose the M -point of the BZ as the origin, giving $\pm \mathbf{K}_D = (\pm 2\pi/3, 0)$ and the valley separation $\mathbf{Q} = 2\mathbf{K}_D = (4\pi/3, 0)$. Eq. 1 with $m = 0$ describes the minimal model of J -layer RG [56], with the pseudospinor defined on the top ($1, A$) and bottom (J, B) layers, $\zeta_J = v^J/\gamma_1^{J-1}$, and $v = \sqrt{3}/2\gamma_0 a_0 \sim 673$ meV nm $^{-1}$, where $\gamma_0 \sim 3.16$ eV and $\gamma_1 \sim 0.445$ eV are the nearest-neighbor intra- and inter-layer hopping parameters [42], respectively, and $a = 0.246$ nm is the graphene lattice constant. To highlight the interplay between band geometry and pairing interactions, we neglect trigonal warping for now and address this aspect later.

The Haldane mass term $m \hat{\sigma}_z \tau_z$ results in a quantum anomalous Hall (QAH) state with a Chern number J [53]. This mass term breaks time-reversal symmetry while preserving inversion symmetry. In contrast, a displacement field produces a sublattice staggered potential $\Delta_V \hat{\sigma}_z$ breaking the inversion symmetry. The band dispersion $\epsilon_{\mathbf{p},J,\pm} = \pm(\zeta_J^2 p^{2J} + m^2)^{1/2}$ near the $\pm \mathbf{K}_D$ points is particle-hole and inversion symmetric. The Bloch wave function for the conduction band near \mathbf{K}_D is $|u_{\mathbf{p}}(\mathbf{K}_D)\rangle = (\cos(\theta_{\mathbf{p}}/2)e^{-i\tau_z J\varphi_{\mathbf{p}}/2}, \sin(\theta_{\mathbf{p}}/2)e^{i\tau_z J\varphi_{\mathbf{p}}/2})$ with $\cos(\theta_{\mathbf{p}}) = m/\epsilon_{\mathbf{p},J,+}$, with inversion symmetry giving $|u_{-\mathbf{p}}(-\mathbf{K}_D)\rangle = \sigma_x |u_{\mathbf{p}}(\mathbf{K}_D)\rangle$. The singularities of the Bloch states near the Dirac points exhibit frustrated momentum-space pseudospin structure, creating a “fertile ground” for spontaneous symmetry breaking [53, 57, 58].

Interaction-induced Haldane phase in RG.—Since our focus is on the superconducting instabilities of the Haldane phase, we consider the simplest case of spinless C2DEGs. In spinless C2DEGs, the corresponding valley-diagonal mass terms are i) $m \hat{\sigma}_z \tau_z$ and ii) $\Delta_V \hat{\sigma}_z$. The latter leads to a valley Hall effect, because time-reversal symmetry ensures that the Berry curvatures at the two valleys are equal in magnitude but opposite in sign. In contrast, the former induces a QAH effect with $\sigma_{xy} = Je^2/h$, since inversion symmetry dictates that the Berry curvatures at the two valleys are identical, resulting in a nontrivial Chern number.

A series of experiments [32, 33, 59, 60] have provided compelling evidence for interaction-driven Haldane phase in RG systems ranging from bilayer to pentalayer. In particular, the QAH conductance is quantized at $5e^2/h$ in pentalayer RG at

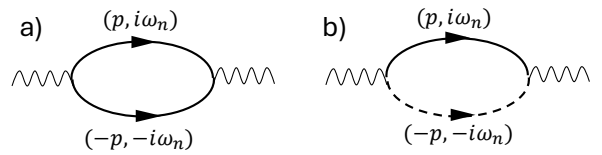


FIG. 2. Feynman diagrams for the a) intra- and b) inter-valley pair susceptibility of chiral 2DEGs. The solid (dotted) lines denote the band projected electron propagator of the \mathbf{K}_D ($-\mathbf{K}_D$) valleys.

zero magnetic field [32]. Effective in these states, only one spin contributes to the QAH effect [53]. Our mean-field analysis for spinless C2DEGs (see End Matter) reveals a negative interaction $u_\perp < 0$ in the $\tau_\perp \equiv \tau \times \tau_z$ channel of the short-ranged valley-dependent interaction leads to a spontaneous QAH state, whereas $u_\perp > 0$ yields a fully-layer-polarized state. The interaction-induced Haldane mass term m depends on the chirality J , which can be significant $m \sim 50$ meV for $J = 4, 5$ for a hBN encapsulated device with a dielectric constant $\epsilon \sim 5$, for gate-screened interactions with gate distance $d = 10$ nm. Since mean-field theory tends to overestimate interaction-induced gaps, we take $m \neq 0$ as a tunable parameter.

Pair susceptibility in the Haldane phase.—One key finding of this Letter is that the pair susceptibility of the Haldane Chern bands is strongly governed by the topologically enforced geometrical properties of the Bloch states, leading to qualitatively distinct superconductivity compared to that of trivial bands. For a generic two-orbital Hamiltonian of the form $H_0 = \hat{\sigma} \cdot \mathbf{h}(\mathbf{k})$, where $\mathbf{h}(\mathbf{k})$ defines the momentum-dependent Hamiltonian field, the projected pair susceptibility $\Pi(\mathbf{q})$ in the σ_0 -channel (see Fig. 2) can be expressed as

$$\Pi(\mathbf{q}) = \int \frac{d^2 \mathbf{k}}{(2\pi)^2} \frac{g(\mathbf{k}, \mathbf{k} + \mathbf{q})}{\xi_{\mathbf{k}+\mathbf{q}} + \xi_{-\mathbf{k}}} \left(\frac{1 + \hat{\mathbf{h}}_{\mathbf{k}+\mathbf{q}} \cdot \hat{\mathbf{h}}_{-\mathbf{k}}}{2} \right), \quad (2)$$

where $\hat{\mathbf{h}}_{\mathbf{k}} = (\hat{h}_x(\mathbf{k}), \hat{h}_y(\mathbf{k}), \hat{h}_z(\mathbf{k}))$ is the normalized Hamiltonian vector field, $\xi_{\mathbf{k}} = \epsilon_{\mathbf{k}} - \mu$ denotes the energy measured from the Fermi surface, and $g(\mathbf{k}, \mathbf{k} + \mathbf{q}) = 1 - n_F(\xi_{\mathbf{k}+\mathbf{q}}) - n_F(\xi_{-\mathbf{k}})$ and $n_F(x) = (e^{\beta x} + 1)^{-1}$ is the Fermi-Dirac distribution with $\beta = 1/(k_B T)$ and \mathbf{k} is defined within the first BZ.

As illustrated in Fig. 1, $\mathbf{q} = 0 + \mathbf{p}$ corresponds to the inter-valley pair susceptibility, whereas $\mathbf{q} = 2\mathbf{K}_D + \mathbf{p}$ denotes the intra-valley pair susceptibility. Due to the topological nature of the band $\hat{\mathbf{h}}_{\mathbf{K}_D} \sim (0, 0, 1)$ and $\hat{\mathbf{h}}_{-\mathbf{K}_D} \sim (0, 0, -1)$, the coherence factors of inter-valley pair susceptibility vanish as $(1 + \hat{\mathbf{h}}_{\mathbf{p}} \cdot \hat{\mathbf{h}}_{-\mathbf{p}})/2 \rightarrow 0$, while the intra-valley pair susceptibility is unaffected, $(1 + \hat{\mathbf{h}}_{\mathbf{p}} \cdot \hat{\mathbf{h}}_{-\mathbf{p}+2\mathbf{K}_D})/2 \rightarrow 1$ (see Fig. 1). Thus, intra-valley pairing remains robust near the $\pm \mathbf{K}_D$, whereas inter-valley pairing is suppressed due to topologically enforced destructive interference of band geometry.

Away from the Dirac points, the intra-valley (S) and inter-valley (D) pair susceptibilities, denoted by $\Pi_S = \Pi(\mathbf{Q} = 2\mathbf{K}_D)$ and $\Pi_D = \Pi(\mathbf{Q} = 0)$, dependent on the ratio of the Haldane

gap m to the Fermi energy μ . They are different for even and odd values of the chiral index J , and can be expressed as

$$\Pi_a = \frac{N_0}{(1-x^2)^\alpha} \log\left(\frac{E_c}{T}\right) f_a(x) + \dots, \quad (3)$$

where \dots denote non-singular terms, $a = S(D)$ denotes the intra- and inter-valley pairing, $N_0 = x^{1-\beta}/(2\pi J\zeta_J^\beta m^{1-\beta})$, denotes the characteristic density-of-states, with $\alpha = 1 - 1/J$, $\beta = 2/J$, $E_c \sim \gamma_1$ is the high-energy cutoff, and we have set the Boltzmann constant $k_B = 1$. The intra-valley (S) and inter-valley (D) pair susceptibilities, depend on $x = m/\mu$ through the functions $f_S(x)$ and $f_D(x)$. For even chirality, $f_S(x) = 1$ and $f_D(x) = (1-x^2)/2$, while for odd chirality $f_S(x) = x^2$ and $f_D(x) = (1-x^2)/2$. Therefore, for even values of J , $\Pi_S > \Pi_D$ throughout the physically relevant range $x \in (0, 1]$. Alternatively, for odd values of J , $\Pi_S > \Pi_D$ requires $x > 1/\sqrt{3}$. In both cases, the geometric suppression of inter-valley coherence represents a hallmark of pairing in the Haldane Chern bands.

When inversion symmetry is explicitly broken, for example, by applying a finite displacement field ($\Delta_V \neq 0$), preserving the topological phase requires $\Delta_V < m$. Simultaneously, realizing two Fermi surfaces, where a distinction between inter- and intra-valley pairing remains meaningful, necessitates $\Delta_V + m < \mu$. Defining $y = \Delta_V/\mu$, these constraints translate into the conditions $y < 1-x$ and $y < x$. In this regime, the intra-valley pair susceptibility becomes valley-dependent and is given by

$$\Pi_S(\pm 2\mathbf{K}_D) = \frac{-N_0}{(1-(x \pm y)^2)^\alpha} \log\left(\frac{E_c}{T}\right) f_S(x \pm y) + \dots. \quad (4)$$

Meanwhile, the inter-valley pair susceptibility loses its weak-coupling logarithmic divergence due to the breaking of inversion symmetry. Finally, in the limit $y > 1-x$ and $y < x$, the system remains in the topological phase but hosts only a single Fermi surface at a single valley. This regime corresponds to a “quarter-metal” superconducting phase [42, 48].

Longitudinal acoustic phonon-mediated pairing.—To determine whether the enhanced intra-valley pair susceptibility leads to an intra-valley superconducting state, we must specify a model for the pairing interaction. Since translational symmetry requires that the pairing interaction is explicitly independent of \mathbf{Q} , any \mathbf{Q} dependence of the pairing interaction must arise from the projection onto the Haldane Chern bands. Our estimates indicate that longitudinal acoustic (LA) phonons provide the leading contribution to the effective pairing interaction for a circular Fermi surface (see End Matter). By employing a continuum model for the electron-phonon coupling and performing a Schrieffer-Wolff transformation on the band-projected interaction, we arrive at the generic form of the effective pairing interaction (see End Matter) with two

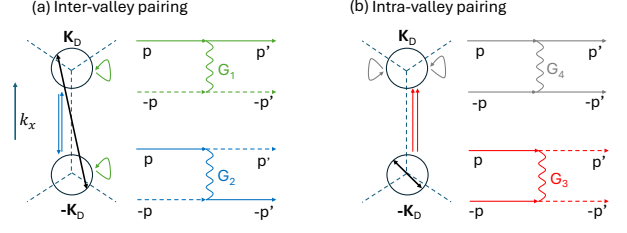


FIG. 3. a) Feynman diagrams for inter-valley scattering interaction G_1 and inter-valley exchange interaction G_2 , and b) Feynman diagrams for intra-valley scattering interaction G_4 and pair tunnelling G_3 . The solid (dotted) lines correspond to the electron propagator in the valley \mathbf{K}_D ($-\mathbf{K}_D$). The colors correspond to the microscopic interactions on the circular Fermi surfaces for both inter-valley and intra-valley pairing.

Fermi surfaces at different valleys,

$$H_{pair} = \sum_{\mathbf{p}, \mathbf{p}'} \left[G_1(\mathbf{p}, \mathbf{p}') a_{\mathbf{p}}^\dagger b_{-\mathbf{p}}^\dagger b_{-\mathbf{p}'} a_{\mathbf{p}'} + G_2(\mathbf{p}, \mathbf{p}') a_{\mathbf{p}}^\dagger b_{-\mathbf{p}}^\dagger a_{-\mathbf{p}'} b_{\mathbf{p}'} \right. \\ \left. + \frac{G_3(\mathbf{p}, \mathbf{p}')}{2} a_{\mathbf{p}}^\dagger a_{-\mathbf{p}}^\dagger b_{-\mathbf{p}'} b_{\mathbf{p}'} + \frac{G_4(\mathbf{p}, \mathbf{p}')}{2} a_{\mathbf{p}}^\dagger a_{-\mathbf{p}}^\dagger a_{-\mathbf{p}'} a_{\mathbf{p}'} \right. \\ \left. + (a \leftrightarrow b) \right], \quad (5)$$

where the electron creation operators at \mathbf{K}_D ($-\mathbf{K}_D$) are defined as $c_{\mathbf{K}_D + \mathbf{p}}^\dagger = a_{\mathbf{p}}^\dagger$ and $c_{-\mathbf{K}_D + \mathbf{p}}^\dagger = b_{\mathbf{p}}^\dagger$. Due to inversion symmetry, the interaction matrix elements $G_i(\mathbf{p}, \mathbf{p}')$, satisfy $G_1(\mathbf{p}, \mathbf{p}') = 2G_4(\mathbf{p}, \mathbf{p}')$ and $G_2(\mathbf{p}, \mathbf{p}') = 2G_3(\mathbf{p}, \mathbf{p}')$. Near the Fermi surface $p_x = p_F \cos(\varphi_{\mathbf{p}})$, $p_y = p_F \sin(\varphi_{\mathbf{p}})$ and $|\mathbf{p}| \sim |\mathbf{p}'| \sim p_F$, the interaction matrix elements can be expressed as,

$$G_4 = -G_0 e^{-J\Phi} \left(\frac{e^{iJ\varphi_{\mathbf{p}}} (\xi_p + \mu - m)}{2(\xi_p + \mu)} + \frac{e^{iJ\varphi_{\mathbf{p}'} (\xi_{\mathbf{p}'} + \mu + m)}}{2(\xi_{\mathbf{p}'} + \mu)} \right)^2, \\ G_3 = -\frac{G_0}{2} \left[1 + (-1)^J \cos(J\Phi) \right] \left(1 - \frac{m^2}{(\xi_p + \mu)^2} \right), \quad (6)$$

where $\Phi = \varphi_{\mathbf{p}} + \varphi_{\mathbf{p}'}$ and the pairing interaction $G_0 = 9.24 \times 10^{-8} (D/(\hbar v_s))^2 \sim 123 \text{ meV}\cdot\text{nm}^{-2}$, with $D \sim 15 \text{ eV}$ denoting the deformation field [61], and $v_s \sim 2 \times 10^4 \text{ m/s}$ is the phonon sound velocity [24, 62]. In Eq. 5, the interactions G_1 and G_2 , which denote inter-valley scattering and inter-valley exchange, as indicated in Fig. 3 a), naturally lead to a conventional superconducting state. Intra-valley pairing results from G_4 and G_3 , which label intra-valley scattering and pair tunnelling between the two valleys, as shown in Fig. 3 b).

To determine the leading pairing instability, we decompose each interaction as $G_{i,l}$ into the angular momentum channels $l = 0, J, -J$. The renormalization group flow equations for the pairing interactions $G_{i,l}$ can be expressed as

$$\dot{g}_{1,l} = -[g_{1,l}^2 + g_{2,l}^2] f_S(x), \quad \dot{g}_{2,l} = -2f_S(x) g_{1,l} g_{2,l}, \quad (7)$$

$$\dot{g}_{4,l} = -[g_{4,l}^2 - g_{3,l}^2] f_D(x), \quad \dot{g}_{3,l} = -2f_D(x) g_{3,l} g_{4,l}, \quad (8)$$

where $g_{i,l}(x) = N_0 G_{i,l} / (1-x^2)^\alpha$ and $\dot{g}_{i,l} = dg_{i,l}/dt$, where $t = \log(\omega_D/T)$ and $\omega_D \sim 0.2 \text{ eV}$ denotes the Debye energy. Eq. 7

and Eq. 8 can be solved by making the substitution $g_{\pm,l}^{intra} = g_{4,l} \pm g_{3,l}$, $g_{\pm,l}^{inter} = g_{1,l} \pm g_{2,l}$ which gives

$$g_{\pm,l}^{intra} = \frac{g_{\pm,l}^{intra}}{1 + f_S(x)g_{\pm,l}^{intra}t}, \quad g_{\pm,l}^{inter} = \frac{g_{\pm,l}^{inter}}{1 + f_D(x)g_{\pm,l}^{inter}t}. \quad (9)$$

The superconducting critical temperature for each pairing channel is determined from the poles of Eq. 9, which depends on the parity of the C2DEG, as discussed below.

For even values of J , the coherence factor $f_D(x) = (1-x^2)/2$ in Eq. 7, arising from the quantum geometric properties of the Haldane phase, leads to the suppression of inter-valley pairing. The critical temperature for the intra-valley (S) pairing (with $f_S(x) = 1$) is $T_c^S(x) = \omega_D \exp(-1/|g_{+,l}^{intra}|)$, higher than that of the inter-valley (D) pairing, $T_c^D(x) = \omega_D \exp(-2/((1-x^2)|g_{+,l}^{intra}|))$. As shown in Fig. 4 a), the ratio T_c^D/T_c^S is exponentially suppressed, indicating that for even parity the intra-valley pairing dominates over the inter-valley pairing for all values of x . This exponential dependence is a direct result of the ratio of the even parity inter- and intra-valley pair susceptibilities Π_D/Π_S as derived in Eq. 3.

Since intra-valley pairing dominates for even values of J we focus on the interaction matrix elements associated with $G_4(\mathbf{p}, \mathbf{p}')$ and $G_3(\mathbf{p}, \mathbf{p}')$. For even chirality J , $(g_{+,l} > g_{-,l})$, with $G_{+,0} = -G_0(1-x^2)$, $G_{+,J} = -G_0(1-x)/2$ and $G_{+,-J} = -G_0(1+x)/2$. As $G_{+,-J} > G_{+,0} > G_{+,J}$ for $x_c > 0.5$ we find that the chiral- J Kekulé superconductor has the largest T_c^S when $k_F \leq (\sqrt{3}m/\zeta_J)^{1/J}$ corresponding to the densities $n_e \leq n_{e,2}$ with $n_{e,2} = 1/(2\pi)(\sqrt{3}m/\zeta_J)^{2/J}$. The superconducting order parameter is given by $\Delta(\mathbf{r}) = \Delta \cos(2\mathbf{K}_D \cdot \mathbf{r} + \theta)$ (where θ corresponds to the relative phase difference between the valleys). Based on the minimal chiral model, we obtain a phase diagram of superconductivity in Fig. 4 b) for even parity chiral 2DEGs in the (n_e, m) parameter space for different values of $J = 4, 6$ and 8 . To ensure a simply connected Fermi surface, we assumed that the electron density $n_e \geq 0.8 \times 10^{12} \text{ cm}^{-2}$, sufficiently large [42, 45] to avoid the three-pocket and annulus Fermi surfaces induced by trigonal warping. Due to the large superfluid stiffness of C2DEGs in the dispersive regime [63], we anticipate the Berezinskii–Kosterlitz–Thouless (BKT) transition temperature T_{BKT}^S to approach the critical mean field temperature $T_{BKT}^S \rightarrow T_c^S$. As detailed in the End Matter, the mean-field critical temperature of the chiral- J Kekulé state is estimated to be in the range $T_c^S \sim 90.8 \text{ mK} - 13.5 \text{ K}$.

The situation is quite different for odd parity chiral 2DEGs, as the intra-valley pairing only dominates the inter-valley pairing when $x > 1/\sqrt{3}$. Therefore, the chiral Kekulé superconducting order has the highest T_c , when $n_e \leq n_{e,1}$ with $n_{e,1} = 1/(2\pi)(\sqrt{2}m/\zeta_J)^{2/J}$. Since $G_{-,-J} = -G_0/2(1+x)$ is the dominant channel for odd parity, the intra-valley pairing order exhibits an π -phase resulting in a Kekulé superconductor with the order parameter $\Delta(\mathbf{r}) = \Delta \sin(2\mathbf{K}_D \cdot \mathbf{r} + \theta)$. $G_{-,-J}$ remains the dominant channel for $1/2 < x < 1/\sqrt{3}$, resulting in a valley-triplet π -phase chiral- J inter-valley superconducting order for the density regime $n_{e,1} < n_e < n_{e,2}$. However,

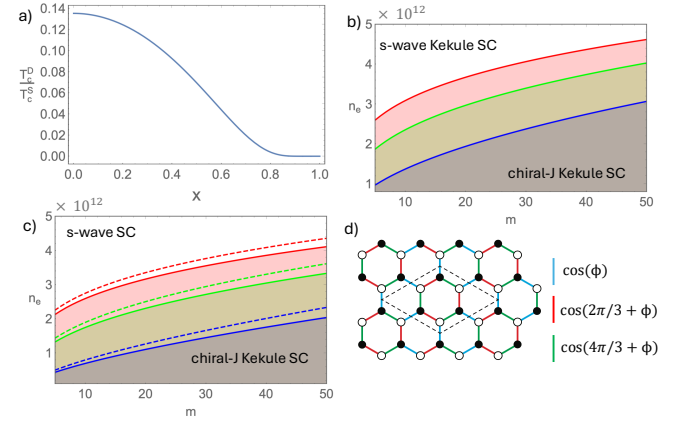


FIG. 4. a) The ratio of the inter-valley critical temperature (T_c^D) to the intra-valley critical temperature (T_c^S) as a function of x . b) Phase diagram for the even chirality C2DEG model of J -layer RG with $J = 4, 6$ and 8 in increasing order. The electron density n_e is in units of cm^{-2} and the Haldane mass is in meV. At low densities, $n_e < n_{e,2}$ the chiral- J Kekulé superconducting channel dominates. c) Phase diagram for the odd chirality C2DEG model of J -layer RG with $J = 3, 5$ and 7 in increasing order, with the same axis label as in b). The chiral- J Kekulé superconducting channel dominates for $n_e < n_{e,2}$, giving way to $\mathbf{Q} = 0$ valley triplet chiral superconductivity for $n_{e,1} < n_e < n_{e,2}$, with the phase boundary indicated by the solid line. Conventional valley singlet s-wave superconductivity dominates for $n_e > n_{e,2}$, with the dashed line indicating the phase boundary. d) Schematic of the Kekulé superconductor on the projected honeycomb lattice, with the superconducting unit cell indicated by the dotted lines.

when $n_e > n_{e,2}$, $G_{+,0} = -G_0(1-x^2)$ becomes the dominant channel, we get a conventional valley singlet s-wave superconductor with $\mathbf{Q} = 0$. Fig. 4 c) shows the phase diagram for the odd parity chiral 2DEGs as a function of (n_e, m) .

Interestingly, for both parities, the presence of a valley degree of freedom permits even-order pairing channels, including a momentum-independent s-wave pairing when $\mu > m$. However, the s-wave pairing channel is suppressed as $\mu \rightarrow m$ given $G_{+,0} = -G_0(1-x^2)$. This suppression originates from a combination of the Pauli exclusion principle and the quantum geometric properties of the Haldane phase. At the Dirac points ($\pm \mathbf{K}_D$), the sublattice and valley degrees of freedom become coincident and act as a single pseudospin, thereby forbidding local (contact) interactions and rendering s-wave Kekulé order incompatible. Consequently, this enhances the relative stability of the chiral- J Kekulé order, which emerges as the dominant channel in this regime. Moreover, due to the presence of a non-zero pair tunnelling channel $G_{3,l}$, we expect the chiral- J Kekulé state to be robust to the application of a displacement field, so long as $\Delta_V < m$.

Chiral Kekulé superconductivity.—The proposed superconducting state exhibits a spatial Kekulé pattern on the projected bipartite lattice, indicated in Fig. 4 d, and notably, the size of the superconducting unit cell is tripled. The odd J -chiral Kekulé superconductor is a valley triplet with the spon-

taneously broken symmetry $U(1) \otimes O_V(3) \otimes \mathbb{Z}_3$, where the $U(1)$ is associated with the overall superconducting phase, $O_V(3)$ is the valley symmetry, and \mathbb{Z}_3 is related to the lattice translational symmetry. Alternatively, the even J -chiral Kekulé superconductor must be a valley singlet with the spontaneously broken symmetry $U(1) \otimes \mathbb{Z}_3$. Unlike the phase-modulated superconductors revealed in the quarter-metal regime [42, 45], the Kekulé superconductors in the half-metal regime are characterized by a spatial modulation of the amplitude of the superconducting order parameter (Fig. 4 d), which can be directly probed using scanning tunneling microscopy.

Kekulé superconducting textures have previously been proposed for Dirac fermions in graphene, arising from nearest-neighbor pairing interactions [54, 64]. However, the mechanism we describe here is fundamentally different: it originates from topologically enforced geometric constraints of the Bloch wavefunctions, which enhances the pair susceptibility at large momenta ($\pm 2\mathbf{K}_D$). As such, this Kekulé superconducting order can emerge from a broad class of attractive interactions in the Haldane phase of C2DEGs, independent of the detailed microscopic pairing mechanism.

In RG, trigonal warping of the bands, due to remote hopping processes, induces Lifshitz transitions [65], wherein the Fermi surface evolves from being circularly connected to an annular Fermi surface or a set of disconnected pockets. For tetralayer RG, this transition occurs in the half-metal regime at an electron density of $n_e \sim 0.4 \times 10^{12} \text{ cm}^{-2}$ near zero displacement field. Even above such a density, where the Fermi surface remains connected, it loses its azimuthal symmetry due to trigonal warping. In the presence of a trigonal warping energy scale E_{tri} , the weak-coupling enhancement of the intra-valley pair susceptibility is cut off by E_{tri} , and Eq. 3 retains the same functional form, but with $\log(E_c/T) \rightarrow \log(E_c/E_{tri})$. Consequently, a critical pairing strength $G_{+,J} = -(1-x^2)^\alpha/(N_0 \log(E_c/E_{tri}))$ is required to stabilize Kekulé superconductivity for even chirality. The general continuum Hamiltonian for a J -layer RG, including remote hopping, can be written as a sum of C2DEG Hamiltonians [66, 67], implying that the chiral index of the Kekulé superconductor can become density dependent. Nevertheless, because the Kekulé superconductivity results from the topologically enforced quantum geometry of the Bloch states, it should be robust against trigonal-warping effects so long as the Fermi surface remains connected.

Multiple superconducting phases have been detected in bilayer to hexalayer RG [44–47] in the fully layer-polarized (FLP) states, induced by displacement fields. However, more recently, superconductivity has been observed in doped layer-antiferromagnetic (LAF) ground states near zero displacement field [46], notably, in the transition region between the FLP and LAF states, where the Haldane phase is expected to occur. In ultra-clean suspended bilayer graphene, an anomalous Hall state with $m \sim 1\text{--}3 \text{ meV}$ has been inferred experimentally [68, 69], while in hBN-encapsulated pentalayer RG devices a QAH state with $m \sim 10\text{--}15 \text{ meV}$ has been reported [32]. It would be valuable to investigate our proposal

for superconducting states arising at zero or small displacement fields within these regimes.

Discussions and Outlook.—In conventional metals, the emergence of PDWs typically requires strong correlation effects or fluctuations tied to lattice-scale physics, often leading to modulation periods incommensurate with the crystalline unit cell [70–87]. In contrast, we showed that in the Haldane phase of C2DEGs, the pair susceptibility is enhanced at finite momentum due to the topologically enforced quantum geometry of the Bloch wavefunctions. This enhancement occurs at high-symmetry points in the Brillouin zone, naturally favoring the formation of lattice-scale PDW states even in the weak-coupling regime. Unlike conventional scenarios that rely on strong-coupling mechanisms, competing orders, or fluctuation-driven instabilities, the quantum geometric mechanism proposed here provides a topologically protected mechanism to realize a lattice-scale PDW order in other chiral Chern bands of 2D crystals and layered materials.

ACKNOWLEDGEMENTS

Work by Y.B. was supported in part by the DOE EPSCoR program under the award DE-SC0022178, and a grant from NIST. F.Z. was supported by the National Science Foundation under grants DMR-2414726, DMR-1945351, and DMR-2324033 and by the Welch Foundation under grant AT-2264-20250403. Work by E.R. was funded by the US Department of Energy, Office of Basic Energy Sciences, via Award DE-SC0022245. Two of us (Y.B. and E.R.) would like to recognize the Kavli Institute for Theoretical Physics (KITP) for hosting us as part of the moire24 program, which is supported by NSF PHY-2309135, where part of this research was performed.

* ybarlas@unr.edu

- [1] Y. Cao, V. Fatemi, S. Fang, K. Watanabe, T. Taniguchi, E. Kaxiras, and P. Jarillo-Herrero, *Nature* **556**, 43 (2018).
- [2] M. Yankowitz, S. Chen, H. Polshyn, Y. Zhang, K. Watanabe, T. Taniguchi, D. Graf, A. F. Young, and C. R. Dean, *Science* **363**, 1059 (2019).
- [3] Y. Cao, V. Fatemi, A. Demir, S. Fang, S. L. Tomarken, J. Y. Luo, J. D. Sanchez-Yamagishi, K. Watanabe, T. Taniguchi, E. Kaxiras, R. C. Ashoori, and P. Jarillo-Herrero, *Nature* **556**, 80 (2018).
- [4] J. M. Park, Y. Cao, K. Watanabe, T. Taniguchi, and P. Jarillo-Herrero, *Nature* **590**, 249 (2021).
- [5] Y. Cao, J. M. Park, K. Watanabe, T. Taniguchi, and P. Jarillo-Herrero, *Nature* **595**, 526 (2021).
- [6] J.-X. Lin, P. Siriviboon, H. D. Scammell, S. Liu, D. Rhodes, K. Watanabe, T. Taniguchi, J. Hone, M. S. Scheurer, and J. I. A. Li, *Nature Physics* **18**, 1221 (2022).
- [7] H. D. Scammell, J. I. A. Li, and M. S. Scheurer, *2D Materials* **9**, 025027 (2022).
- [8] Y. Xia, Z. Han, K. Watanabe, T. Taniguchi, J. Shan, and K. F. Mak, *Nature* **637**, 833 (2025).

[9] Y. Guo, J. Pack, J. Swann, L. Holtzman, M. Cothrine, K. Watanabe, T. Taniguchi, D. G. Mandrus, K. Barmak, J. Hone, A. J. Millis, A. Pasupathy, and C. R. Dean, *Nature* **637**, 839 (2025).

[10] G. W. Burg, E. Khalaf, Y. Wang, K. Watanabe, T. Taniguchi, and E. Tutuc, *Nature Materials* **21**, 884 (2022).

[11] H. Zhou, L. Holleis, Y. Saito, L. Cohen, W. Huynh, C. L. Patterson, F. Yang, T. Taniguchi, K. Watanabe, and A. F. Young, *Science* **375**, 774 (2022).

[12] T. J. Peltonen, R. Ojaajarvi, and T. T. Heikkilä, *Phys. Rev. B* **98**, 220504 (2018).

[13] H. C. Po, L. Zou, A. Vishwanath, and T. Senthil, *Phys. Rev. X* **8**, 031089 (2018).

[14] C. Xu and L. Balents, *Phys. Rev. Lett.* **121**, 087001 (2018).

[15] J. F. Dodaro, S. A. Kivelson, Y. Schattner, X. Q. Sun, and C. Wang, *Phys. Rev. B* **98**, 075154 (2018).

[16] X. Y. Xu, K. T. Law, and P. A. Lee, *Phys. Rev. B* **98**, 121406 (2018).

[17] C.-C. Liu, L.-D. Zhang, W.-Q. Chen, and F. Yang, *Phys. Rev. Lett.* **121**, 217001 (2018).

[18] H. Isobe, N. F. Q. Yuan, and L. Fu, *Phys. Rev. X* **8**, 041041 (2018).

[19] J. González and T. Stauber, *Phys. Rev. Lett.* **122**, 026801 (2019).

[20] T. Cea, N. R. Walet, and F. Guinea, *Phys. Rev. B* **100**, 205113 (2019).

[21] Y.-Z. Chou, F. Wu, J. D. Sau, and S. Das Sarma, *Phys. Rev. Lett.* **127**, 217001 (2021).

[22] V. o. T. Phong, P. A. Pantaleón, T. Cea, and F. Guinea, *Phys. Rev. B* **104**, L121116 (2021).

[23] F. Wu, A. H. MacDonald, and I. Martin, *Phys. Rev. Lett.* **121**, 257001 (2018).

[24] F. Wu, E. Hwang, and S. Das Sarma, *Phys. Rev. B* **99**, 165112 (2019).

[25] B. Lian, Z. Wang, and B. A. Bernevig, *Phys. Rev. Lett.* **122**, 257002 (2019).

[26] Y. W. Choi and H. J. Choi, *Phys. Rev. B* **98**, 241412 (2018).

[27] R. Ojaajarvi, T. Hyart, M. A. Silaev, and T. T. Heikkilä, *Phys. Rev. B* **98**, 054515 (2018).

[28] T. Cea and F. Guinea, *Proceedings of the National Academy of Sciences* **118**, e2107874118 (2021).

[29] E. Khalaf, S. Chatterjee, N. Bultinck, M. P. Zaletel, and A. Vishwanath, *Science Advances* **7**, eabf5299 (2021).

[30] T. Han, Z. Lu, G. Scuri, J. Sung, J. Wang, T. Han, K. Watanabe, T. Taniguchi, H. Park, and L. Ju, *Nature Nanotechnology* **19**, 181 (2024).

[31] Z. Lu, T. Han, Y. Yao, A. P. Reddy, J. Yang, J. Seo, K. Watanabe, T. Taniguchi, L. Fu, and L. Ju, *Nature* **626**, 759 (2024).

[32] T. Han, Z. Lu, Y. Yao, J. Yang, J. Seo, C. Yoon, K. Watanabe, T. Taniguchi, L. Fu, F. Zhang, and L. Ju, *Science* **384**, 647 (2024).

[33] Y. Sha, J. Zheng, K. Liu, H. Du, K. Watanabe, T. Taniguchi, J. Jia, Z. Shi, R. Zhong, and G. Chen, *Science* **384**, 414 (2024).

[34] Z. Lu, T. Han, Y. Yao, Z. Hadjri, J. Yang, J. Seo, L. Shi, S. Ye, K. Watanabe, T. Taniguchi, and L. Ju, *Nature* **637**, 1090 (2025).

[35] A. Jahin and S.-Z. Lin, *Enhanced kohn-luttinger topological superconductivity in bands with nontrivial geometry* (2024), arXiv:2411.09664.

[36] M. Kim, A. Timmel, L. Ju, and X.-G. Wen, *Phys. Rev. B* **111**, 014508 (2025).

[37] Y.-Z. Chou, J. Zhu, and S. D. Sarma, *Intravalley spin-polarized superconductivity in rhombohedral tetralayer graphene* (2024), arXiv:2409.06701.

[38] M. Geier, M. Davydova, and L. Fu, *Chiral and topological superconductivity in isospin polarized multilayer graphene* (2024), arXiv:2409.13829.

[39] H. Yang and Y.-H. Zhang, *Topological incommensurate fulde-ferrell-larkin-ovchinnikov superconductor and bogoliubov fermi surface in rhombohedral tetra-layer graphene* (2024), arXiv:2411.02503.

[40] Y.-Q. Wang, Z.-Q. Gao, and H. Yang, *Chiral superconductivity from parent chern band and its non-abelian generalization* (2024), arXiv:2410.05384.

[41] Q. Qin and C. Wu, *Chiral finite-momentum superconductivity in the tetralayer graphene* (2024), arXiv:2412.07145.

[42] C. Yoon, T. Xu, Y. Barlas, and F. Zhang, *Quarter metal superconductivity* (2025), arXiv:2502.17555 [cond-mat.mes-hall].

[43] G. Parra-Martinez, A. Jimeno-Pozo, V. T. Phong, H. Sainz-Cruz, D. Kaplan, P. Emanuel, Y. Oreg, P. A. Pantaleon, J. A. Silva-Guillen, and F. Guinea, *Band renormalization, quarter metals, and chiral superconductivity in rhombohedral tetralayer graphene* (2025), arXiv:2502.19474 [cond-mat.str-el].

[44] H. Zhou, T. Xie, T. Taniguchi, K. Watanabe, and A. F. Young, *Nature* **598**, 434 (2021).

[45] T. Han, Z. Lu, Z. Hadjri, L. Shi, Z. Wu, W. Xu, Y. Yao, A. A. Cotten, O. Sharifi Sedeh, H. Weldeyesus, J. Yang, J. Seo, S. Ye, M. Zhou, H. Liu, G. Shi, Z. Hua, K. Watanabe, T. Taniguchi, P. Xiong, D. M. Zumbühl, L. Fu, and L. Ju, *Nature* [10.1038/s41586-025-09169-7](https://doi.org/10.1038/s41586-025-09169-7) (2025).

[46] M. Kumar, D. Waleffe, A. Okounkova, R. Tejani, V. T. Phong, K. Watanabe, T. Taniguchi, C. Lewandowski, J. Folk, and M. Yankowitz, (2025), arXiv:2507.18598 [cond-mat.mes-hall].

[47] E. Morissette, P. Qin, H.-T. Wu, N. J. Zhang, R. Q. Nguyen, K. Watanabe, T. Taniguchi, and J. I. A. Li, (2025), arXiv:2504.05129 [cond-mat.mes-hall].

[48] S. A. Mursheed and B. Roy, *Phys. Rev. B* **112**, 085121 (2025).

[49] G. Jiang and Y. Barlas, *Phys. Rev. Lett.* **131**, 016002 (2023).

[50] G. D. Mahan, *Many-particle physics* (Plenum Press New York, 1981) pp. xiv, 1003 p.

[51] J. B. Ketterson and S. N. Song, *Superconductivity* (Cambridge University Press, 1999).

[52] P. Coleman, *Introduction to Many-Body Physics* (Cambridge University Press, 2015).

[53] F. Zhang, J. Jung, G. A. Fiete, Q. Niu, and A. H. MacDonald, *Phys. Rev. Lett.* **106**, 156801 (2011).

[54] B. Roy and I. F. Herbut, *Phys. Rev. B* **82**, 035429 (2010).

[55] From here onward, we use the term haldane phase to refer to the QAH phase induced by the mass term $m\hat{\sigma}_z\tau_z$ in C2DEGs, even though the microscopic mechanism leading to this phase can vary depending on the chirality index J .

[56] H. Min and A. H. MacDonald, *Phys. Rev. B* **77**, 155416 (2008).

[57] H. Min, G. Borghi, M. Polini, and A. H. MacDonald, *Phys. Rev. B* **77**, 041407 (2008).

[58] F. Zhang, H. Min, M. Polini, and A. H. MacDonald, *Phys. Rev. B* **81**, 041402 (2010).

[59] F. R. Geisenhof, F. Winterer, A. M. Seiler, J. Lenz, T. Xu, F. Zhang, and R. T. Weitz, *Nature* **598**, 53 (2021).

[60] F. Winterer, F. R. Geisenhof, N. Fernandez, A. M. Seiler, F. Zhang, and R. T. Weitz, *Nature Physics* **20**, 422 (2024).

[61] We adopt a conservative estimate for the deformation field, noting that it can be up to twice as large [24, 62]. A detailed study is required to determine different electron–phonon scattering processes that can contribute to the magnitude of the deformation field for each J -layer RG system.

[62] Y.-Z. Chou, F. Wu, J. D. Sau, and S. Das Sarma, *Phys. Rev. Lett.* **127**, 187001 (2021).

[63] X. Hu, E. Rossi, and Y. Barlas, *Phys. Rev. B* **112**, 144502 (2025).

- [64] J. P. L. Faye, M. N. Diarra, and D. Sénéchal, [Phys. Rev. B](#) **93**, 155149 (2016).
- [65] F. Zhang, B. Sahu, H. Min, and A. H. MacDonald, [Phys. Rev. B](#) **82**, 035409 (2010).
- [66] M. Koshino and E. McCann, [Phys. Rev. B](#) **80**, 165409 (2009).
- [67] S. Slizovskiy, E. McCann, M. Koshino, and V. I. Fal'ko, [Communications Physics](#) **2**, 164 (2019).
- [68] J. Martin, B. E. Feldman, R. T. Weitz, M. T. Allen, and A. Yacoby, [Phys. Rev. Lett.](#) **105**, 256806 (2010).
- [69] F. Freitag, J. Trbovic, M. Weiss, and C. Schönenberger, [Phys. Rev. Lett.](#) **108**, 076602 (2012).
- [70] A. Himeda, T. Kato, and M. Ogata, [Phys. Rev. Lett.](#) **88**, 117001 (2002).
- [71] F. Loder, A. P. Kampf, and T. Kopp, [Phys. Rev. B](#) **81**, 020511 (2010).
- [72] P. A. Lee, [Phys. Rev. X](#) **4**, 031017 (2014).
- [73] R. Soto-Garrido and E. Fradkin, [Phys. Rev. B](#) **89**, 165126 (2014).
- [74] E. Fradkin, S. A. Kivelson, and J. M. Tranquada, [Rev. Mod. Phys.](#) **87**, 457 (2015).
- [75] D. F. Agterberg, J. S. Davis, S. D. Edkins, E. Fradkin, D. J. Van Harlingen, S. A. Kivelson, P. A. Lee, L. Radzihovsky, J. M. Tranquada, and Y. Wang, [Annual Review of Condensed Matter Physics](#) **11**, 231 (2020).
- [76] Z. Han, S. A. Kivelson, and H. Yao, [Phys. Rev. Lett.](#) **125**, 167001 (2020).
- [77] X. Liu, Y. X. Chong, R. Sharma, and J. C. S. Davis, [Science](#) **372**, 1447 (2021).
- [78] E. Berg, E. Fradkin, E.-A. Kim, S. A. Kivelson, V. Oganesyan, J. M. Tranquada, and S. C. Zhang, [Phys. Rev. Lett.](#) **99**, 127003 (2007).
- [79] D. F. Agterberg and H. Tsunetsugu, [Nature Physics](#) **4**, 639 (2008).
- [80] E. Berg, E. Fradkin, S. A. Kivelson, and J. M. Tranquada, [New Journal of Physics](#) **11**, 115004 (2009).
- [81] D. F. Agterberg and J. Garaud, [Phys. Rev. B](#) **91**, 104512 (2015).
- [82] Y. Wang, S. D. Edkins, M. H. Hamidian, J. C. S. Davis, E. Fradkin, and S. A. Kivelson, [Phys. Rev. B](#) **97**, 174510 (2018).
- [83] Z. Dai, Y.-H. Zhang, T. Senthil, and P. A. Lee, [Phys. Rev. B](#) **97**, 174511 (2018).
- [84] S. D. Edkins, A. Kostin, K. Fujita, A. P. Mackenzie, H. Eisaki, S. Uchida, S. Sachdev, M. J. Lawler, E.-A. Kim, J. C. S. Davis, and M. H. Hamidian, [Science](#) **364**, 976 (2019).
- [85] D. F. Agterberg, M. Sigrist, and H. Tsunetsugu, [Phys. Rev. Lett.](#) **102**, 207004 (2009).
- [86] S. Baruch and D. Orgad, [Phys. Rev. B](#) **77**, 174502 (2008).
- [87] M. R. Norman and J. C. S. Davis, [Proceedings of the National Academy of Sciences](#) **115**, 5389 (2018).
- [88] C.-X. Liu, Y. Chen, A. Yazdani, and B. A. Bernevig, [Phys. Rev. B](#) **110**, 045133 (2024).

End Matter

Interaction effects in J-layer RG.—For long-range interactions that are both valley- and spin-independent, the spontaneously broken symmetry quantum valley Hall (QVH) and quantum anomalous Hall (QAH) phases are energetically degenerate. To distinguish between these competing states, one must consider interactions that break valley symmetry or differentiate between the sublattices. Since both QVH and QAH mass terms share the same sublattice structure but differ in their valley dependence, only valley-dependent interactions can lift their degeneracy. Therefore, we only include valley-dependent interactions in our analysis.

The interacting Hamiltonian, $H_{int} = H_{ee} + H'_{int}$, includes the SU(4) Coulomb interaction H_{ee} , with the Coulomb repulsion $v_{\mathbf{q}}$, and the valley-dependent interaction H'_{int}

$$H_{int} = \frac{1}{2L^2} \sum_{\mathbf{k}, \mathbf{k}', \mathbf{q}} v_{\mathbf{q}} \psi_{\mathbf{k}+\mathbf{q}}^\dagger \psi_{\mathbf{k}} \psi_{\mathbf{k}'-\mathbf{q}}^\dagger \psi_{\mathbf{k}'} + \frac{1}{2L^2} \sum_{\mathbf{k}, \mathbf{k}', \mathbf{q}} \sum_{\mu=x,y,z} u_{\mu} \psi_{\mathbf{k}+\mathbf{q}}^\dagger \hat{\tau}_{\mu} \psi_{\mathbf{k}} \psi_{\mathbf{k}'-\mathbf{q}}^\dagger \hat{\tau}_{\mu} \psi_{\mathbf{k}'}, \quad (10)$$

where u_{μ} 's are short ranged valley-dependent interaction terms. $\hat{\tau}_z$ acts on the valley degree of freedom and L^2 denotes the sample area. For simplicity, we assume that $u_x = u_y = u_{\perp}$.

To perform the mean-field theory, we rewrite the Hamiltonian H by adding and subtracting the mean field terms $H_{\hat{\Delta}}$ as $H = (H_0 + H_{\hat{\Delta}}) + (H_{int} - H_{\hat{\Delta}}) = H_{MF} + H_{res}$, and H_0 corresponds to the non-interacting Hamiltonian. The mean-field Hamiltonian H_{MF} is treated as the non-perturbative Hamiltonian, and the effect of H_{res} can be studied via a diagrammatic approach. To ensure the field $\hat{\Delta}$ is self-consistently determined, we satisfy the tree-level self-consistent equation corresponding to the Feynman diagrams shown in Fig. 5. We consider the competition between interaction-induced mass terms, one corresponding to the QAH effect, m , and the other to the QVH effect, Δ . The QVH Hamiltonian $H_{QVH} = \sum_{\mathbf{k}} \psi_{\mathbf{k}}^\dagger \Delta_{VH} \hat{\sigma}_z \psi_{\mathbf{k}}$, and the QAH Hamiltonian as $H_{QAH} = \sum_{\mathbf{k}} \psi_{\mathbf{k}}^\dagger m \hat{\sigma}_z \hat{\tau}_z \psi_{\mathbf{k}}$ where $\hat{\sigma}_z$ acts on the sublattice degree of freedom. In the presence of valley anisotropy, the self-consistent gap equation at the tree level becomes

$$\hat{\Delta} = -\frac{1}{\beta} \sum_n \int \frac{d^2 k'}{(2\pi)^2} \left[v_{\mathbf{k}-\mathbf{k}'} G_{MF}(\mathbf{k}', i\omega_n) + \sum_{\mu=x,y} u_{\mu} \hat{\tau}_{\mu} G_{MF}(\mathbf{k}', i\omega_n) \hat{\tau}_{\mu} \right], \quad (11)$$

$$\frac{v_{\mathbf{k}-\mathbf{k}'}}{\tau_{\mu}} + \sum_{\mu=x,y} \frac{u_{\perp}}{\tau_{\mu}} = -\hat{\Delta}$$

FIG. 5. Tree-level Feynmann diagram corresponding to the self-consistent solution to the gap equation for the mean field $\hat{\Delta}$.

where $G_{MF}(\mathbf{k}) = (i\omega_n - H_{MF}(\mathbf{k}))^{-1}$ is the Green's function associated with the mean-field Hamiltonian, $\omega_n = (2n + 1)\pi/\beta$ and $\beta = 1/(k_B T)$. Performing the summation over the frequencies, we arrive at the gap equations:

$$m(\mathbf{k}) = \int \frac{d^2 k'}{(2\pi)^2} \left[v_{\mathbf{k}-\mathbf{k}'} - 2u_{\perp} \right] \frac{m(\mathbf{k}')} {2E_{\mathbf{k}'}} \tanh \left(\frac{\beta E_{\mathbf{k}'}}{2} \right), \quad (12)$$

$$\Delta_{VH}(\mathbf{k}) = \int \frac{d^2 k'}{(2\pi)^2} \left[v_{\mathbf{k}-\mathbf{k}'} + 2u_{\perp} \right] \frac{\Delta_{VH}(\mathbf{k}')} {2E_{\mathbf{k}'}} \tanh \left(\frac{\beta E_{\mathbf{k}'}}{2} \right),$$

where $E_{\mathbf{k}}^2 = |\epsilon_{J,\mathbf{k}}|^2 + m_{\mathbf{k}}^2$ for the QAH state, and $E_{\mathbf{k}}^2 = |\epsilon_{J,\mathbf{k}}|^2 + \Delta_{VH}(\mathbf{k})^2$ for the QVH state. From the structure of Eqs. 12, it is clear that only u_{\perp} lifts the degeneracy of the QAH and QVH state; therefore, we take $u_z = 0$. The above equations imply that the QAH is preferred over the QVH state for $u_{\perp} < 0$. The negative sign that distinguishes the QAH state from the QVH state is due to the anti-commutation of the Pauli matrices, in the valley space $\hat{\tau}_z \hat{\tau}_x = -\hat{\tau}_x \hat{\tau}_z$ and $\hat{\tau}_z \hat{\tau}_y = -\hat{\tau}_y \hat{\tau}_z$.

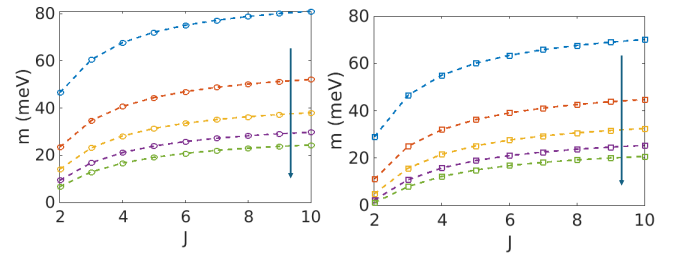


FIG. 6. Interaction induced mass gaps for different chirality indices J for a) long-range Coulomb interactions and b) gate-screened interaction with $d = 10$ nm evaluated at the Dirac point with a cutoff $k_c = \gamma_1/(\hbar v)$. Each curve corresponds to a different value of the dielectric constant $\epsilon = 5, 7.5, 10, 12.5$ and 15 , from the top to bottom, with an arrow indicating the direction of increasing ϵ .

Fig. 6 a) shows the interaction-induced mass gaps as a function of the chirality index J for the bare Coulomb interaction $v_{\mathbf{q}} = 2\pi e^2/(\epsilon q)$ and $u_{\perp} < 0$ ($|u_{\perp}| \sim 2$ meV) computed for different values of the dielectric constant $\epsilon = 5, 7.5, 10, 12.5$ and 15 . In the self-consistent calculation, we impose a momentum cutoff $k_c = \gamma_1/v$ and evaluate m at the Dirac point $\mathbf{k} = 0$. For low dielectric screening (e.g., $\epsilon = 5$), the interaction-induced mass gaps are substantial, with $m > 50$ meV. For reference, the dielectric constant of h-BN is approximately $\epsilon \sim 6$. As expected, increasing the dielectric screening reduces the magnitude of the induced gaps. To account for the influence of nearby metallic gates, we incorporate a gate-screened Coulomb interaction $v_{\mathbf{q}}^{sc} = v_{\mathbf{q}} \tanh(qd/2)$ where d is the distance between the gates. The results are plotted in Fig. 6 b). Even in the presence of gate screening, the mass gaps remain sizable for $\epsilon = 5$, particularly in tetra- and pentalayer graphene, where we find $m > 50$ meV.

Pair susceptibility in other channels—One can calculate the particle-particle susceptibility in the $\hat{\sigma}_z$ channel. Here, we restrict to even chiralities. Again estimating the leading logarithmic contribution one finds, $\Pi_{-S} = x^2 \Pi_S$ and $\Pi_{-D} =$

$(1 - x^2)/2\Pi_S$, where $\Pi_{-S}(\Pi_{-D})$ are the inter- and intra-valley pair susceptibility in the σ_z -channel (Π_S denotes the even J intra-valley pair susceptibility). The intra-valley pair susceptibility exceeds the inter-valley counterpart for $x \geq 1/\sqrt{3}$, indicating that in the $\hat{\sigma}_z$ channel intra-valley Kekulé superconductivity should be favored when $\mu \leq \sqrt{3}m$. One can also evaluate the pair susceptibility in the $\hat{\sigma}_x$ and $\hat{\sigma}_y$ channels for the Haldane phase. Here, we find that the inter-valley susceptibility dominates over the intra-valley component.

Longitudinal acoustic phonons.—The longitudinal acoustic (LA) phonons in RG correspond to in-phase motion of the low-energy unstacked Carbon atoms (1A, JB). For J -layer RG, both the intra-layer acoustic and optical modes contribute to a total of 2^J longitudinal phonon modes, with 2^{J-1} LA phonon and 2^{J-1} longitudinal optical (LO) phonon modes. We assume that inter-layer phonon coupling is weak, and express the continuum limit of the electron-phonon coupling (EPC) Hamiltonian as,

$$H_{EPC} = D \int d\mathbf{r} \nabla U(\mathbf{r}) \sum_{\alpha=1A,JB} \psi_{\alpha}^{\dagger}(\mathbf{r}) \psi_{\alpha}(\mathbf{r}), \quad (13)$$

where $D \sim 15$ eV is the effective deformation potential $U(\mathbf{r})$ is the deformation field [24, 62]. To proceed, we move to momentum space, quantize the deformation potential in terms of bosonic operators $b_{\mathbf{q}}(b_{-\mathbf{q}}^{\dagger})$,

$$U(\mathbf{r}) = \sum_{\mathbf{q}} \left(\frac{\hbar}{2NM\omega_{\mathbf{q}}} \right)^{1/2} e^{i\mathbf{q}\cdot\mathbf{r}} (b_{\mathbf{q}} + b_{-\mathbf{q}}^{\dagger}), \quad (14)$$

where N denotes the number of unit cells, M is the mass of the Carbon atom, and we assume an isotropic phonon dispersion $\omega_{\mathbf{q}} = v_s q$. To determine the pairing interaction mediated by LA phonons, we worked in the band basis $c_{\mathbf{k},m}^{\dagger} = \sum_{\alpha} u_{m\alpha}^{\star}(\mathbf{k}) c_{\mathbf{k}\alpha}^{\dagger}$, where m denotes the band index, and performed a Schriffer-Wolff transformation (with $\eta = D(\hbar L^2/(2NM\omega_q))^{1/2}$) on the band-projected electron-phonon interaction. The effective pairing Hamiltonian H_{pair} for the BCS pair $(\mathbf{k} + \mathbf{Q}; -\mathbf{k} + \mathbf{Q})$ with a center of mass momentum $2\mathbf{Q}$, takes the form

$$H_{pair} = \frac{1}{L^2} \sum_{\mathbf{k},\mathbf{k}',\mathbf{Q}} V_{\mathbf{k},\mathbf{k}',\mathbf{Q}} c_{\mathbf{k}+\mathbf{Q}}^{\dagger} c_{-\mathbf{k}+\mathbf{Q}}^{\dagger} c_{-\mathbf{k}'+\mathbf{Q}} c_{\mathbf{k}'+\mathbf{Q}}, \quad (15)$$

with an effective interaction

$$V_{\mathbf{k},\mathbf{k}',\mathbf{Q}} = -A_{uc} \left(\frac{D}{\hbar v_s} \right)^2 \frac{\hbar^2}{2M} \Gamma_{\mathbf{k},\mathbf{k}',\mathbf{Q}} = -G_0 \Gamma_{\mathbf{k},\mathbf{k}',\mathbf{Q}}, \quad (16)$$

where A_{uc} is the area of the unit cell, and we neglect the retardation effect of the pairing interaction, and

$$\Gamma_{\mathbf{k},\mathbf{k}',\mathbf{Q}} = \langle u_{m,\mathbf{k}+\mathbf{Q}} | u_{m,\mathbf{k}'+\mathbf{Q}} \rangle \langle u_{m,-\mathbf{k}+\mathbf{Q}} | u_{m,-\mathbf{k}'+\mathbf{Q}} \rangle, \quad (17)$$

encodes the effect of band geometry on the effective pairing interaction. Notice that with the assumption of a linear phonon dispersion, the magnitude of the effective interaction $G_0 \sim 123$ meV nm $^{-2}$ becomes \mathbf{Q} independent.

The Fermi surfaces consist of two electron-like or hole-like pockets below (above) or above (below) half-filling of the valence (conduction) bands. We treat the Fermi surfaces as circular, which are separated by $2\mathbf{Q} = (4\pi/3, 0)$. The effective pairing interaction can be divided into four types G_1, G_2, G_3 , and G_4 , which are related due to inversion symmetry (see Eq. 5 and Fig. 3 and subsequent discussion in the text). The intra-valley interactions G_4 and G_3 can be expressed as,

$$G_4 = -G_0 \langle u_{\mathbf{K}_D/2}(\mathbf{p}) | u_{\mathbf{K}_D/2}(\mathbf{p}') \rangle \langle u_{\mathbf{K}_D/2}(\mathbf{p}) | u_{\mathbf{K}_D/2}(\mathbf{p}') \rangle, \quad (18)$$

$$G_3 = -G_0 \langle u_{\mathbf{K}_D/2}(\mathbf{p}) | u_{-\mathbf{K}_D/2}(\mathbf{p}') \rangle \langle u_{\mathbf{K}_D/2}(\mathbf{p}) | u_{-\mathbf{K}_D/2}(\mathbf{p}') \rangle,$$

which can be evaluated using the Bloch wavefunctions of the C2DEG.

Our analysis indicates that optical phonon-mediated pairing, proposed as a possible mechanism in twisted bilayer graphene [23, 25, 88], is weaker than the LA phonon-mediated interaction. The estimated strength of the optical phonon-induced pairing interaction is approximately ~ 70 meV nm $^{-2}$ [23], about half that of the LA phonon-mediated counterpart. Consequently, we neglect its contribution in our analysis. We note, however, that because optical phonons correspond to out-of-phase oscillations between the two sublattices within the unit cell, they generate an off-diagonal electron-phonon coupling that favors inter-valley pairing (see the discussion above).

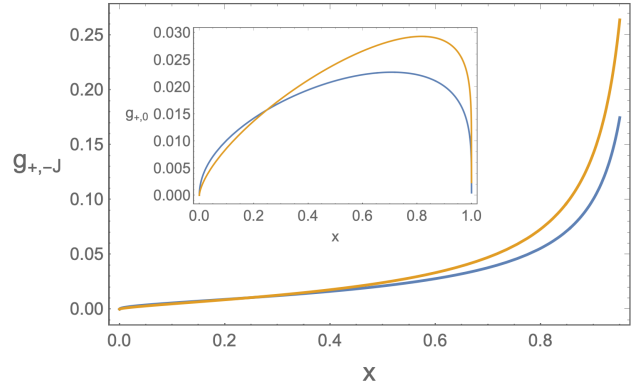


FIG. 7. $g_{+,J}$ as a function of x for a Haldane mass $m = 10$ meV, for $J = 4$ and 6 in increasing order, with the inset corresponding to $g_{+,0}$.

Critical Temperature scaling.—The critical temperature $T_c(x)$ for the even parity chiral- J Kekulé superconductor is determined by $g_{+,J}$, whereas the s-wave Kekulé superconductor is determined by $g_{+,0}$. Fig. 7 shows the behavior of $g_{+,J}(g_{+,0})$ as a function of x for $J = 4$ and 6 , with a Haldane mass $m = 10$ meV. As $x \rightarrow 1$, $g_{+,J}$ increases sharply, due to the large density of states at the bottom of the band, while $g_{+,0} \rightarrow 0$ due to suppression of the s-wave channel. At $x = 0.5$, we find $g_{0,-J} > g_{+,0}$, resulting in the s-wave Kekulé superconducting phase at higher densities. Using $\omega_D \sim 0.2$ eV and $g_{+,J} \sim 0.1 - 0.2$, for $J = 4, 6$, yields $T_c^S \sim 90.8$ mK – 13.5 K for the chiral- J Kekulé superconductor.